


Multifunctional Asymmetric Sound Manipulations by a Passive Phased Array Prism

Yin Wang,¹ Jian-ping Xia,¹ Hong-xiang Sun,^{1,2,3,*} Shou-qi Yuan,¹ Yong Ge,¹ Qiao-ru Si,¹ Yi-jun Guan,¹ and Xiao-jun Liu^{2,3,†}

¹*Research Center of Fluid Machinery Engineering and Technology, Faculty of Science, Jiangsu University, Zhenjiang 212013, China*

²*Key Laboratory of Modern Acoustics, Department of Physics and Collaborative Innovation Center of Advanced Microstructures, Nanjing University, Nanjing 210093, China*

³*State Key Laboratory of Acoustics, Institute of Acoustics, Chinese Academy of Sciences, Beijing 100190, China*

 (Received 6 September 2018; revised manuscript received 21 July 2019; published 16 August 2019)

We report the theoretical and experimental realization of four types of passive phased array prisms with various asymmetric acoustic manipulations (AAMs) in air. The designed prisms consist of 31 transmitted unit cells of phase manipulation, which are composed of a n layer symmetric Helmholtz resonator (SHR) unit cell. Based on asymmetric phase distributions created by the nonparallel characteristic of exit interfaces on both sides of the structures, we can design a passive prism with asymmetric acoustic transmission (AAT) in which its fractional bandwidth can reach about 0.26. More interestingly, by adjusting the parameter of the SHR unit cells in the prism, we realize three other types of AAMs with the same mechanism, such as bidirectional acoustic insulation, asymmetric acoustic focusing, and reversed AAT. The proposed prisms have the advantages of broad bandwidth, multifunctional AAM, and passive structure as well as being easy to fabricate, and have great potential applications in integrated sound devices.

DOI: [10.1103/PhysRevApplied.12.024033](https://doi.org/10.1103/PhysRevApplied.12.024033)

I. INTRODUCTION

Recent years have witnessed rapidly increasing attention in the study of unidirectional wave manipulation due to its potential applications in a wide range of fields. For electromagnetic waves, several concepts based on magnetic biasing enable to break reciprocity and realize unidirectional optical manipulation by using both linear [1–8] and nonlinear [9–12] mechanisms. Taking inspiration from developments in electromagnetism, unidirectional acoustic manipulation (UAM) has also become a hot topic because of its extensive applications in many important fields, such as medical ultrasound and architectural acoustics.

Acoustic diode devices opened up a method to achieve UAM by breaking the time-reversal symmetry with nonlinear systems [13,14]. However, the efficiency of frequency conversion for nonlinear systems is generally low. To overcome this limitation, use of an active acoustic metamaterial [15], a relatively broadband UAM device with subwavelength thickness and high performance, was experimentally demonstrated. Beyond that, a circulating fluid in a resonant ring cavity [16] was introduced as the role of electron spin to mimic an effective magnetic field for acoustics and

to realize UAM by breaking the time-reversal symmetry [17–20]. Despite the great achievements that have been made in this area, it suffers great challenges to achieve UAM with more complex functionality because of fabrication complexities and accurate control of the fluid velocity. In addition to UAM, the concept of asymmetric manipulation in optics [21–25] and acoustics [26–48] with many distinct features and high performance has attracted increasing attention. In the acoustic community, emerging sonic crystals (SCs) and acoustic metamaterials have provided several alternative schemes to design systems with asymmetric acoustic transmission (AAT) based on asymmetric structure configurations and other characteristics, such as diffraction by grating structures [26–30], Bragg scattering by SCs [31–35], abnormal refraction by near-zero-index or high-index materials [36,37], and so on. Besides these AAT structures, acoustic metasurfaces [38–40] have recently become a research focus and have provided design possibilities for AAT devices with planar ultrathin structures [41–48]. As examples, the AAT tunnel [41] and window [42,43] are designed by attaching a pair of acoustic metasurfaces inside waveguide structures. In free space, the AAT and asymmetric acoustic focusing (AAF) effects can be obtained based on dual-layer metasurfaces with asymmetric phase modulation [44–46], lossy metasurfaces [47], and coding metasurfaces

*jsdxshx@ujs.edu.cn

†liuxiaojun@nju.edu.cn

[48]. In these types of metasurfaces, the double-layer metasurface is capable of realizing multiple asymmetric acoustic manipulations (AAMs) based on the asymmetric phase modulation of both metasurfaces, while the double-layer structure inevitably leads to difficulties in device integration. Generally, it is very difficult to realize asymmetric manipulations in a single layer of metasurface due to the same phase distribution on both sides. Thus, the design of a monolayer passive structure with asymmetric phase modulation still remains a great technical challenge.

In this work, we propose four types of passive prisms based on 31 transmitted unit cells of phase manipulation, which consist of a n layer symmetric Helmholtz resonator (SHR) unit cell to realize different discrete phase delays. Based on asymmetric phase distributions created by the nonparallel characteristic of exit interfaces on both sides of the structures, the AAT prism with a fractional bandwidth of 0.26 is realized both numerically and experimentally. Moreover, by adjusting the parameter of the SHR unit cell, three other types of phased array prisms with different AAMs, such as bidirectional acoustic insulation (BAI), AAF, and reversed AAT are also successively demonstrated. The experimental measurements match well with the numerical results.

II. THEORETICAL MODEL OF AAT PRISM

As shown in Fig. 1(a), we design an AAT prism, which consists of 31 passive phased arrays with a width l . The shape of the AAT prism is an isosceles triangle with the bottom angle $\alpha = 45^\circ$ and a height H . The abbreviations BI and TI represent the normal incidence of acoustic waves from the bottom and top sides of the prism, respectively. Figures 1(a) and 1(b) show the acoustic propagation paths through the AAT prism for BI and TI, respectively, in which the prism is placed in region II. For BI, the acoustic wave can pass through the prism with a refraction angle θ_{t1} , but the transmitted acoustic energy is confined on the left and right exit surfaces with $\theta_{t1} = -90^\circ$. Moreover, in the range $-90^\circ < \theta_{t1} \leq \alpha - 90^\circ$, the acoustic wave can

transmit through the prism, but cannot reach region I. Here, we only analyze the left half of the prism due to its structural symmetry, and the left exit surface is defined as the x_1 axis. Based on the generalized Snell's law [49], we can obtain

$$\sin \theta_t = \frac{d\varphi}{kdx}, \quad (1)$$

where $k = 2\pi f/c$ is the wave number in air and c and f are the acoustic velocity and the frequency, respectively. In the case of BI, the acoustic phase delay φ_1 created by the prism in the x_1 direction is given as

$$\varphi_1 = \sqrt{2} \sin \theta_{t1} k(H + x). \quad (2)$$

Based on Eq. (2), the phase delays between two adjacent unit cells ($\Delta\varphi_1$) can be calculated as

$$\Delta\varphi_1 = \sqrt{2} \sin \theta_{t1} kl. \quad (3)$$

For TI, the acoustic wave can pass through the prism and reach region III with a refraction angle θ_{t2} [shown in Fig. 1(b)], and the bottom exit surface is defined as the x_2 axis. Based on Eq. (3), the phase delays between two adjacent unit cells ($\Delta\varphi_2$) can be calculated as

$$\Delta\varphi_2 = \sqrt{2} \sin \theta_{t1} kl - kl + 2\pi m, \quad (4)$$

where $2\pi m$ is selected to keep the phase difference between two adjacent unit cells in the range of 2π , satisfying the generalized Snell's law. The acoustic phase delay φ_2 in the x_2 direction for TI is expressed as

$$\varphi_2 = \sqrt{2} \sin \theta_{t1} k(H + x) - kx + 2\pi m \frac{H + x}{l}. \quad (5)$$

Based on Eq. (1), the relationship between the refraction angles θ_{t2} and θ_{t1} can be written as

$$\sin \theta_{t2} = \sqrt{2} \sin \theta_{t1} - 1 + \frac{2\pi m}{kl}. \quad (6)$$

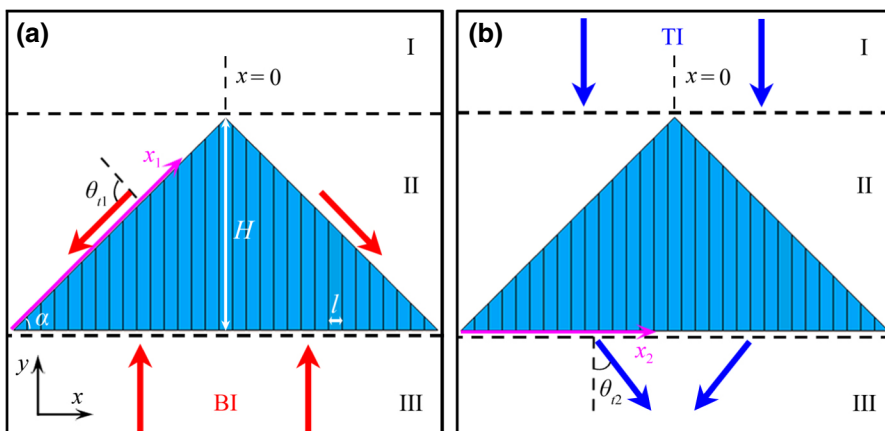


FIG. 1. Propagation paths through the AAT prism with different phase distributions for (a) BI and (b) TI. The refraction angles θ_{t1} and θ_{t2} correspond to BI and TI, respectively.

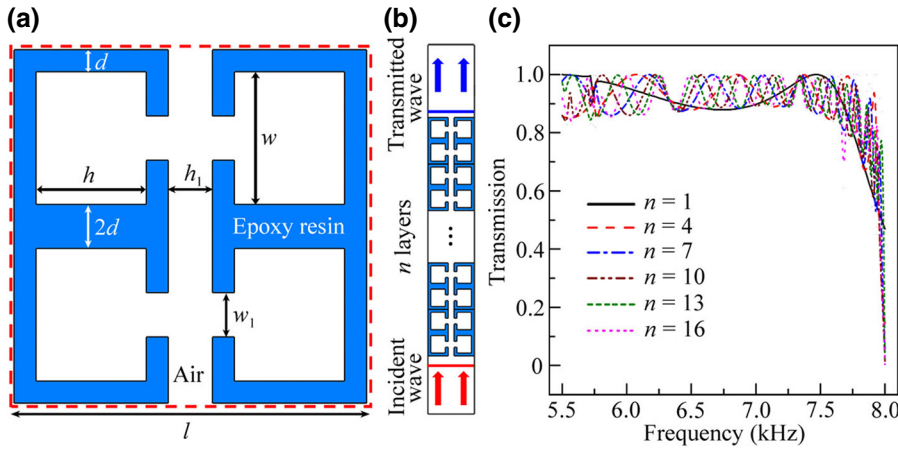


FIG. 2. Schematic of (a) a SHR unit cell and (b) a transmitted unit cell of phase manipulation composed of a n layer SHR unit cell. (c) Transmission spectra of the transmitted unit cells with different numbers (n) of SHR unit cell.

The aforementioned results show that the phase distributions of the exit surfaces in the prism are different for BI and TI, and so do the refraction angles θ_{t1} and θ_{t2} , indicating the feasibility of designing the AAT prism.

III. DESIGN AND PERFORMANCES OF AAT PRISM

A. SHR unit cell

To design the AAT prism, we propose a type of square unit cell (with length $l=16$ mm) composed of two SHRs and a central straight pipe with a tunable width of h_1 immersed in air. As shown in Fig. 2(a), the cavity width h_2 is determined by the pipe width h_1 , and the other parameters are selected as $d=1.0$ mm, $h_2=(l-4d-h_1)/2$, $w_1=1.5$ mm, and $w_2=(l-4d)/2$. The SHR unit cell is fabricated with epoxy resin to satisfy the sound hard-boundary condition. In this work, the finite element method based on COMSOL Multiphysics software is utilized to numerically simulate the AAM characteristics. The material parameters are adopted as follows: the density $\rho=1180$ kg/m³, the longitudinal wave velocity $c_l=2720$ m/s, and the transversal wave velocity $c_t=1460$ m/s for the epoxy resin; $\rho_a=1.21$ kg/m³ and $c_a=343$ m/s for air.

As shown in Fig. 2(b), we design a transmitted unit cell of phase manipulation composed of a n layer SHR unit cell with $h_1=5.2$ mm in which the incident acoustic wave is located at the bottom side. Figure 2(c) shows the transmission spectra with different numbers of SHR unit cells, in which n is selected as 1, 4, 7, 10, 13, and 16. It is found that with the increase of n , the transmission spectra have similar shapes, and the transmissions are larger than 0.85 in the range from 5.5 to 7.7 kHz, indicating the broadband characteristic of the transmitted unit cell.

B. Design of AAT prism

We design an AAT prism based on the SHR unit cell in which the phase gradient of the prism in the x_1 direction is selected as $d\varphi_1/kdx_1=-1.0$, and thus the refraction angle θ_{t1} can be calculated as -90° . To obtain the required phase delay of a single SHR unit cell in the AAT prism, we first theoretically calculate the phase delays based on Eq. (3), which is shown as the blue solid line in Fig. 3(a). In addition, we simulate the actual phase delays of a single SHR unit cell with different frequencies [red dashed line in Fig. 3(a)]. Note that the theoretically calculated phase delay is the same as that of the SHR unit cell at 6.66 kHz [black dot in Fig. 3(a)]. Based on Eq. (6), we also calculate

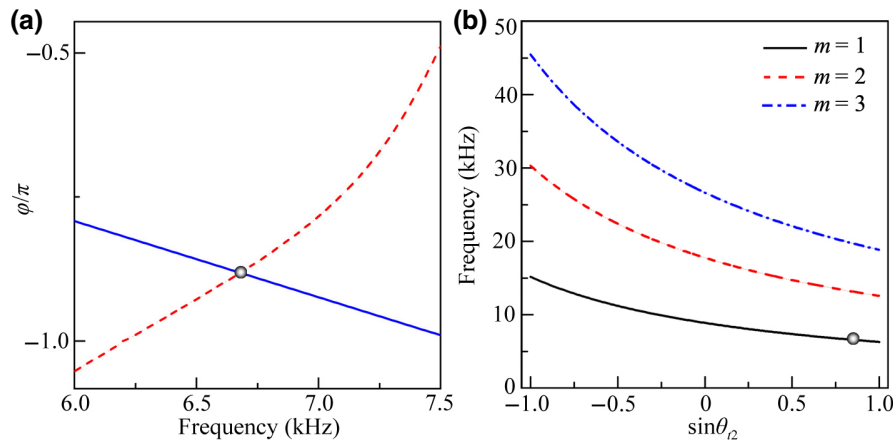


FIG. 3. (a) Theoretically calculated phase delays (blue solid line) based on Eq. (3) and actual phase delays (red dashed line) of a single SHR unit cell with different frequencies. The refraction angle θ_{t1} is selected as -90° . (b) The parameter $\sin\theta_{t2}$ at different frequencies for $m=1, 2$, and 3. The frequencies of the black dots in (a),(b) are 6.66 kHz.

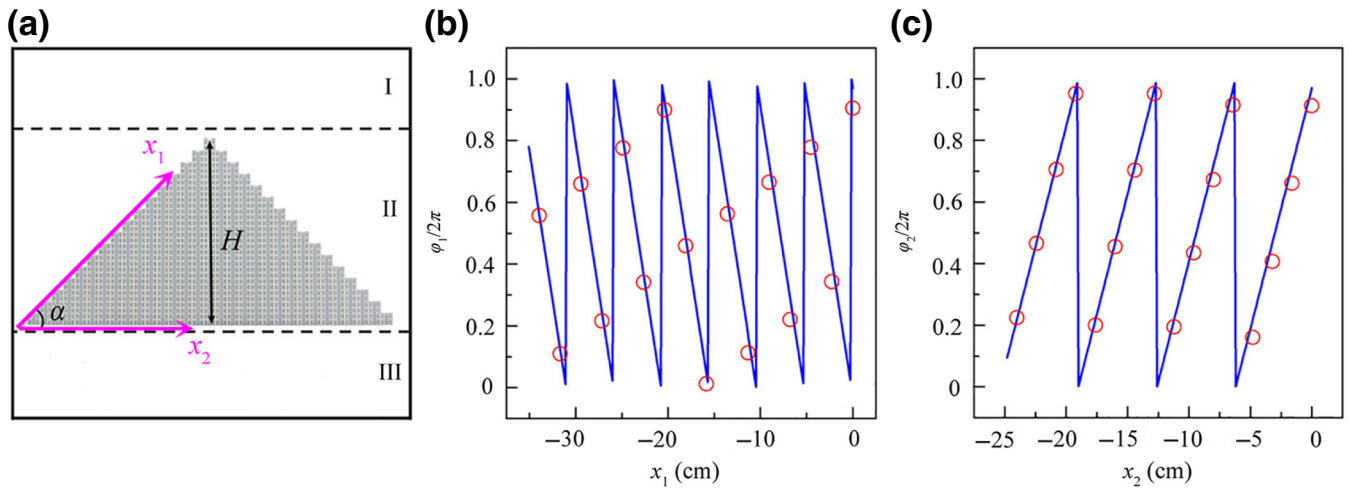


FIG. 4. (a) Photograph of the AAT prism. Theoretical continuous (blue solid lines) and discrete (red open circles) phase delays in (b) x_1 and (c) x_2 directions of the AAT prism at 6.66 kHz.

the parameter $\sin\theta_{t2}$ at different frequencies for $m = 1, 2,$ and 3 [Fig. 3(b)], and the parameters m and θ_{t2} are obtained as 1 and 54° at 6.66 kHz [black dot in Fig. 3(b)], respectively. Therefore, based on the SHR unit cell and these parameters, we can design the AAT prism with $\theta_{t1} = -90^\circ$ and $\theta_{t2} = 54^\circ$ for BI and TI, respectively.

Figure 4(a) shows the photograph of the designed AAT prism composed of 31 transmitted unit cells of phase manipulation in which the central transmitted unit cell

consists of the 16 SHR unit cells, and the number of the SHR unit cells in other transmitted unit cells on the both side gradually decreases. The parameters of all SHR unit cells are the same as those in Fig. 2(a). Based on this, we design the AAT prism with $\alpha = 45^\circ$ and $H = 25.6$ cm, and the other parameters are selected as $f = 6.66$ kHz, $m = 1,$ $c = 343$ m/s, $\theta_{t1} = -90^\circ,$ and $\theta_{t2} = 54^\circ$. By using Eqs. (2) and (5), we can calculate the theoretical continuous phase delays (blue solid lines) in the x_1 and x_2 directions of the

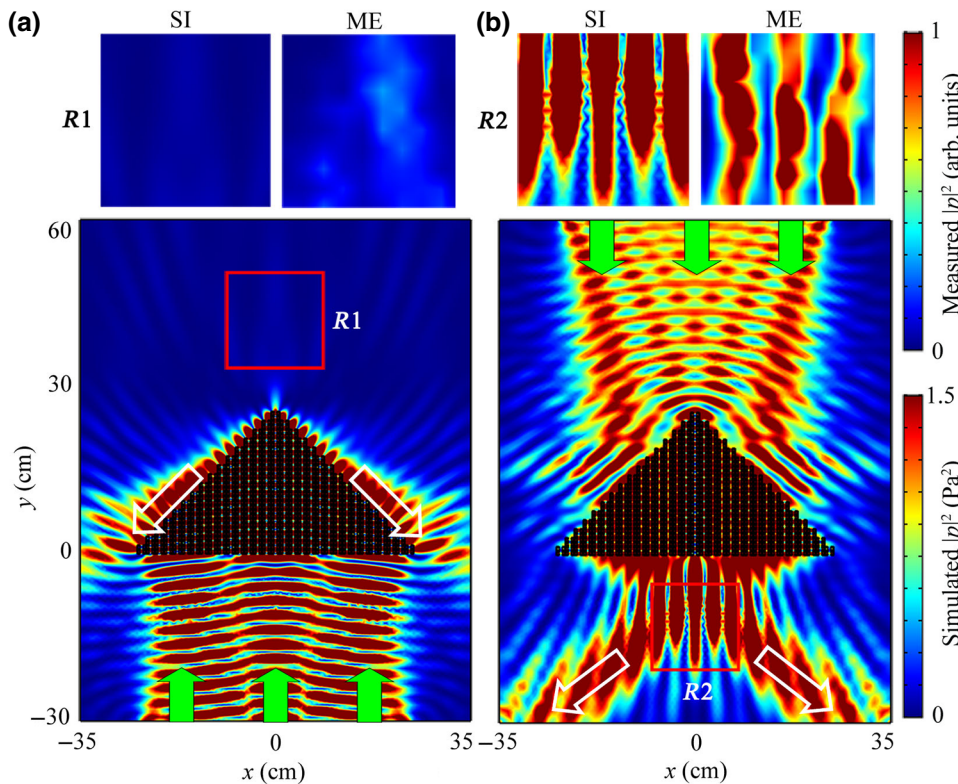


FIG. 5. Simulated distributions of acoustic intensity field induced by the AAT prism for (a) BI and (b) TI at 6.66 kHz. Measured (ME) and simulated (SI) distributions of intensity field in the red squares $R1$ and $R2$ are shown in the top region. White open and green solid arrows represent the theoretical refraction and incident directions, respectively.

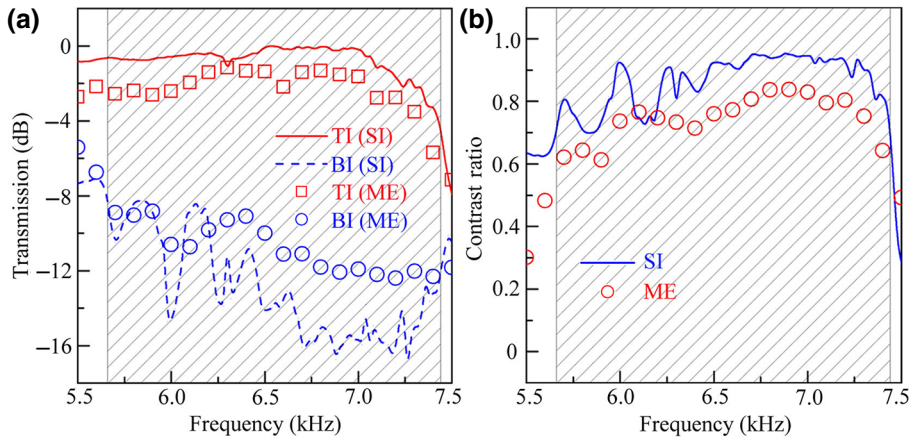


FIG. 6. (a) Simulated and measured transmission spectra of the prism for BI and TI and (b) contrast ratios versus frequency. Black shaded regions (from 5.66 to 7.44 kHz) represent the working band of the AAT.

AAT prism at 6.66 kHz, which are shown in Figs. 4(b) and 4(c), respectively. In addition, 16 discrete phase delays of the transmitted unit cells (red open circles) in the x_1 and x_2 directions are displayed due to the symmetry structure of the prism. Note that the phase distributions of the AAT prism are different in the x_1 and x_2 directions, and the discrete phase delays agree well with the theoretical ones in both directions.

C. Performances of AAT prism

Figures 5(a) and 5(b) show the simulated distributions of the intensity field ($|p|^2$) induced by the AAT prism at 6.66 kHz for BI and TI, respectively. As shown in Fig. 5(a), the transmitted acoustic energy is confined on both exit surfaces and cannot reach region I. But for TI, the acoustic wave can transmit through the prism and reach region III, showing an obvious AAT phenomenon. The simulated

refraction angles for BI and TI are the same as the theoretical values ($\theta_{r1} = -90^\circ$ and $\theta_{r2} = 54^\circ$, white open arrows). Therefore, we deduce that the proposed prism with an asymmetric phase distribution can realize AAT with a high performance.

To verify the AAT performance, we also measure the intensity distributions for BI and TI in the red squares R1 and R2 (with a size of $16 \times 16 \text{ cm}^2$) in Fig. 5. The experimental setup and sample photographs are presented in Appendix A. As shown in the upper four insets of Figs. 5(a) and 5(b), for both BI and TI, the measured and simulated results agree well with each other, and thus the AAT performance of the prism is experimentally demonstrated.

D. Bandwidth of AAT prism

To quantitatively present the bandwidth of the AAT prism, we simulate the transmission spectra of the prism for BI and TI. Here, we define the transmission as P/P_0 , where P_0 and P are the integration of the acoustic intensity in the same regions without and with the prism, respectively, and the selected integration regions are regions I and III for BI and TI, respectively. As shown in Fig. 6(a), the transmissions are lower than -8 dB for BI in the black shaded region, while the transmissions are larger than -4 dB for TI in which the transmission spectra show remarkable AAT behavior. Beyond that, we experimentally measure the transmission spectra for BI and TI, which agree with the simulated results in the shaded region. However, there exists a small difference in the transmission spectra between the measured and simulated results. This is because the measured transmission spectra are obtained by measuring and integrating the intensity of several lines and the corresponding intensity distribution is nonuniform.

To further evaluate the AAT performance, we introduce the contrast ratio defined as $R_c = |P_T - P_B| / (P_T + P_B)$, in which P_T and P_B are the integration of acoustic intensity induced by the prism for TI and BI, respectively.

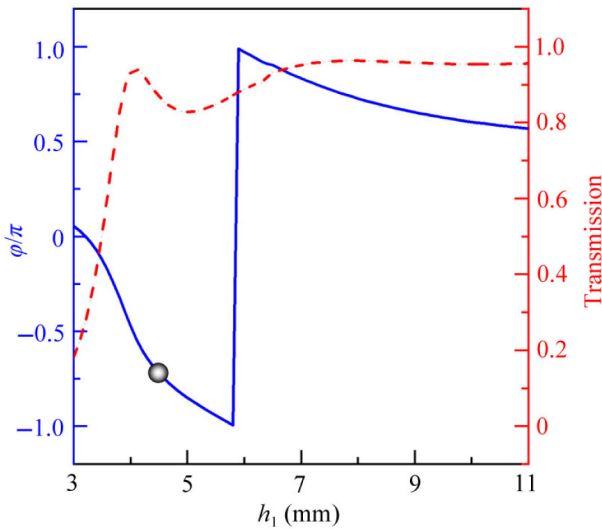


FIG. 7. Phase delays (blue solid line) and transmissions (red dashed line) of a single SHR unit cell with different values of h_1 at 6.66 kHz. The black dot corresponds to $h_1 = 4.5 \text{ mm}$, which is used to design the BAI prism.

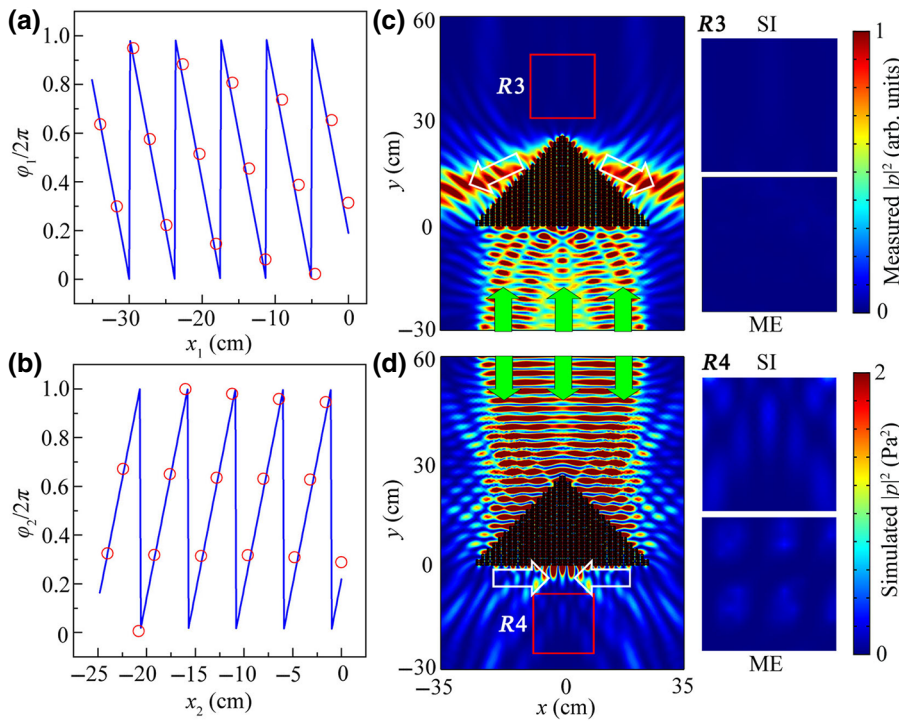


FIG. 8. Theoretical continuous (blue solid line) and discrete (red open circles) phase delays of the BAI prism with $h_1 = 4.5$ mm in (a) x_1 and (b) x_2 directions. Simulated distributions of acoustic intensity field induced by the BAI prism for (c) BI and (d) TI. Measured and simulated distributions of acoustic intensity field in the red squares R3 and R4 are shown in the right region. White open and green solid arrows refer to theoretical refraction and incident directions, respectively.

The absolute value of R_c represents the relative weight of transmitted sound energy between TI and BI. As shown in Fig. 6(b), the simulated R_c is larger than 0.7 in the black shaded region, indicating that the bandwidth of the AAT prism is about 1.78 kHz, and its fractional bandwidth can reach about 0.26. The experimental measurements are also plotted for comparison, which are slightly lower than

the simulated results due to the small difference of the transmission spectra in Fig. 6(a).

Furthermore, we simulate the distributions of the acoustic intensity field induced by the AAT prism for TI and BI at the other three frequencies in the shaded region, which are shown in Appendix B. It is found that by changing the incident frequency, the AAT effect still exists, but the

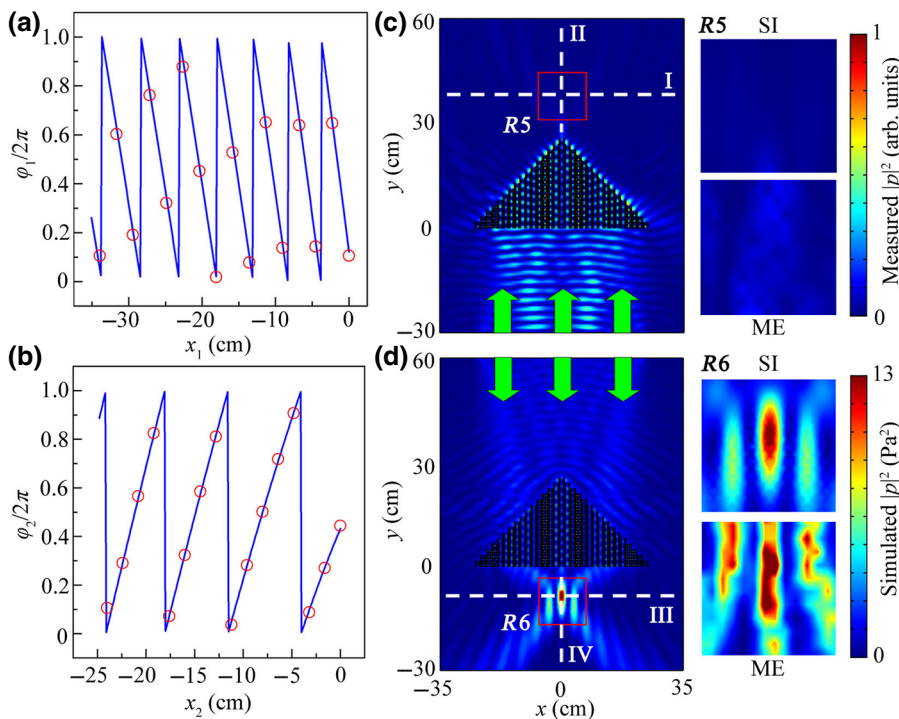


FIG. 9. Theoretical continuous (blue solid line) and discrete (red open circles) phase delays of the AAF prism in (a) x_1 and (b) x_2 directions at 6.66 kHz. Simulated distributions of acoustic intensity field induced by the AAF prism for (c) BI and (d) TI. Measured and simulated distributions of acoustic intensity field in the red squares R5 and R6 are presented in the right region. Green solid arrows in (c),(d) refer to the incident direction.

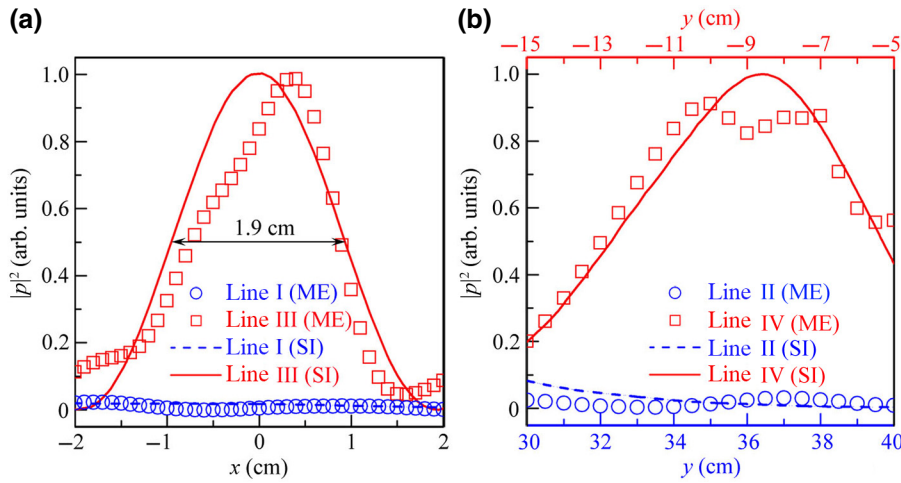


FIG. 10. Measured and simulated acoustic intensity profiles along (a) lines I and III and (b) lines II and IV in Fig. 9.

refraction angles of the transmitted waves for BI and TI change simultaneously.

In addition to the aforementioned results, we discuss the influence of the parameter w_2 of the SHR unit cell on the AAT performances of the prism, which is shown in Appendix C. Similar to the results with different incident frequencies, the AAT effect can be obtained with the change of the parameter w_2 , but the refraction angles of the transmitted waves on both side of the prism also change simultaneously. Therefore, the transmitted refraction angles for BI and TI can be manipulated by the incident frequency and the parameter w_2 .

IV. DESIGN AND PERFORMANCES OF OTHER TYPES OF PRISMS

A. BAI prism

In addition to the AAT prism, we can realize three other types of AAM prisms (such as BAI, AAF, and reversed AAT) by changing parameter h_1 of the SHR unit cell. Figure 7 shows the phase delays (blue solid line) and transmissions (red dashed line) of a single SHR unit cell with different values of h_1 at 6.66 kHz. Note that with the increase of h_1 , the phase delay can cover the range of 1.5π , and the transmissions are larger than 0.8 in the range 3.8–11.0 mm.

To design the BAI prism, the refraction angles for BI and TI should satisfy $-90^\circ \leq \theta_{t1} \leq -45^\circ$ and $\theta_{t2} = 90^\circ$, respectively. Here, we select the phase gradient as $d\varphi_2/kdx_2 = 1.0$ in the x_2 direction of the BAI prism, and the theoretical refraction angles can be calculated as $\theta_{t2} = 90^\circ$ and $\theta_{t1} = -59^\circ$ based on Eqs. (1) and (6). The simulated results of the BAI prism are shown in Supplemental Material [50] in which the prism can basically realize the BAI phenomenon at 6.66 kHz. However, part of the sound energy is not strictly confined on the bottom surface of the prism for TI due to the insufficient number of the transmitted unit cells in the BAI prism.

To better confine the transmitted energy on the bottom surface for TI, we further increase the phase gradient in the x_2 direction by $d\varphi_2/kdx_2 = 1.05$. By using the selected phase gradient, the transmitted acoustic wave is converted into an evanescent surface wave for TI [49]. Based on Eqs. (3) and (6), we theoretically obtain $\theta_{t1} = -56^\circ$ and $h_1 = 4.5$ mm (black dot in Fig. 7) at 6.66 kHz. Therefore, we theoretically calculate the distributions of the phase delay of the prism in the x_1 and x_2 directions based on Eqs. (2) and (5), which agree well with the corresponding discrete phase delays of the transmitted unit cells [shown in Figs. 8(a) and 8(b)].

Figures 8(c) and 8(d) show the simulated distributions of the intensity field induced by the BAI prism with $h_1 = 4.5$ mm for BI and TI, respectively, in which the other parameters are the same as those in Fig. 5. It is found that the acoustic refraction angle for BI is the same as its theoretical value ($\theta_{t1} = -56^\circ$, white open arrows). In addition, compared with the results with $d\varphi_2/kdx_2 = 1.0$, the transmitted acoustic energy for TI presents a typical characteristic of the evanescent wave and is better confined on the bottom surface of the prism [shown in Fig. 8(d)]. Moreover, the measured acoustic intensity distributions in the red rectangles $R3$ and $R4$ are also displayed in the right region. The measured results agree well with the simulated ones, showing great BAI performance.

B. AAF prism

Next, we design the AAF prism based on 31 transmitted unit cells with different parameter h_1 of the SHR unit cell (shown in the Supplemental Material [50]), in which the other parameters of the prism are the same as those in Fig. 5. Here, the focusing effect corresponds to the case of TI, and thus we choose $\sin\theta_{t2} = (-x_2)/\left(\sqrt{x_2^2 + e^2}\right)$, where $e = 0.2$ m is the focal length. Based on Eqs. (2), (5), and (6), we can theoretically calculate the phase distributions (blue solid lines) of the prism in the x_1 and

x_2 directions, which are shown in Figs. 9(a) and 9(b), respectively. In addition, the red open circles represent the discrete phase delays of the 16 selected transmitted unit cells in the x_1 and x_2 directions, and the parameter h_1 of each transmitted unit cell is shown in the Supplemental Material [50]. Figures 9(c) and 9(d) show the simulated distributions of the acoustic intensity field at 6.66 kHz for BI and TI, respectively, exhibiting an obvious AAF phenomenon. Note that the acoustic wave can transmit through the AAF prism for TI and the transmitted acoustic energy is focused on a point. But for BI, the transmitted sound energy is very weak. This is because the calculated $d\varphi_1/kdx_1$ in the x_1 direction is in the range from -0.95 to -1.22 (shown in the Supplemental Material [50]). Therefore, the refraction angle θ_{t1} of part of the transmitted wave is around -90° , and the other part is converted into an evanescent wave, which cannot reach region I for BI. Moreover, the measured acoustic intensity fields in the red squares *R5* and *R6* are also displayed at the right side for comparison, which agrees well with the corresponding simulated results.

Furthermore, the measured and simulated results of the normalized intensity profiles along lines I–IV [shown in Figs. 9(c) and 9(d)] are displayed in Fig. 10. Note that the acoustic intensities along lines III and IV are much larger than those along lines I and II. In addition, the full width at half maximum of the focus in the x direction [shown in Fig. 10(a)] is about 1.9 cm (about $0.36\lambda_0$). The measured results match well with the simulated ones. Both experimental and numerical results demonstrate that the designed

AAF prism has good subwavelength-focusing and AAT performances.

C. Reversed AAT prism

Finally, we also design a reversed AAT prism whose performance is opposite to that of the previously designed AAT prism. In the reversed AAT prism, the acoustic wave can transmit through the prism for BI, but cannot pass through the prism for TI. To realize such a performance, we first select $d\varphi_2/kdx_2 = -1.0$, and the theoretical refraction angle can be calculated as $\theta_{t2} = -90^\circ$, $\theta_{t1} = 0^\circ$, and $m = 0$ based on Eqs. (1) and (6). The parameter h_1 of each transmitted unit cell and the simulated AAT performances of the reversed prism are shown in the Supplemental Material [50]. Similar to the results of the BAI prism with $d\varphi_2/kdx_2 = 1.0$, part of the sound energy is not strictly confined on the bottom surface of the prism for TI. To further optimize the AAT performance, we further increase the phase gradient in the x_2 direction by $d\varphi_2/kdx_2 = -1.1$, and thus the transmitted wave for TI is converted into the evanescent wave [49].

Based on Eqs. (2), (5), and (6), we can obtain $\theta_{t1} = -4^\circ$ and $m = 0$ and calculate the phase distributions of the reversed AAT prism in the x_1 and x_2 directions, which are shown in Figs. 11(a) and 11(b), respectively. The red open circles represent the discrete phase delays of the 16 transmitted unit cells in which the corresponding parameter h_1 of each transmitted unit cell in the reversed AAT prism is shown in the Supplemental Material [50]. Figures 11(c)

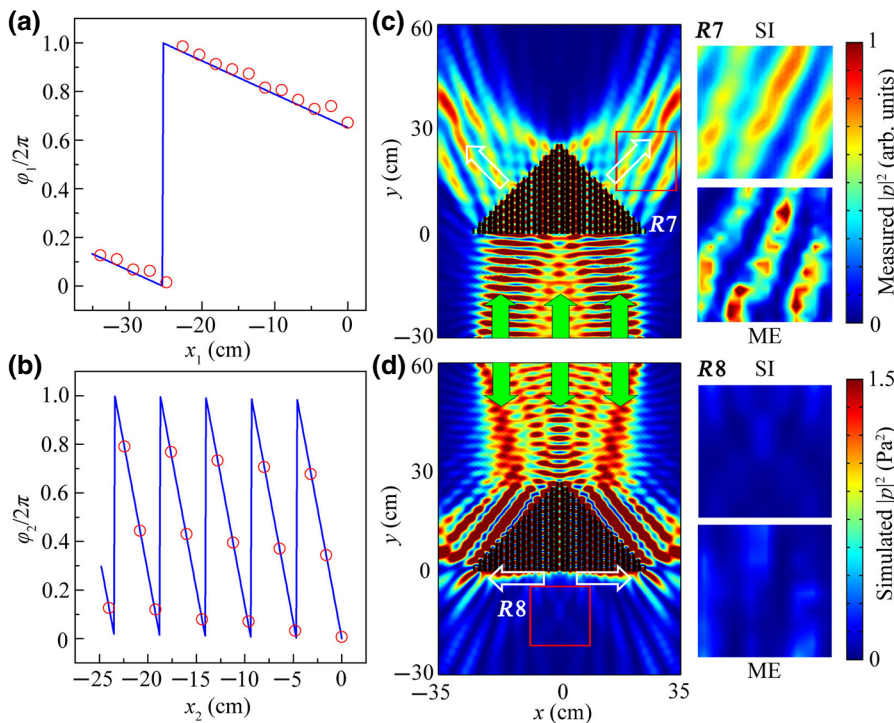


FIG. 11. Theoretical continuous (blue solid lines) and discrete (red open circles) phase delays of the reversed AAT prism in (a) x_1 and (b) x_2 directions at 6.66 kHz. Simulated distributions of acoustic intensity field induced by the reversed AAT prism for (c) BI and (d) TI. Measured and simulated distributions of acoustic intensity field in red squares *R7* and *R8* are presented in the right region. White open and green solid arrows refer to theoretical refraction and incident directions, respectively.

and 11(d) show the simulated distributions of the intensity field induced by the AAT prism for BI and TI at 6.66 kHz, respectively. Contrary to the results in Fig. 5, the acoustic wave can transmit through the prism and reach region I for BI, while the acoustic wave is confined on the bottom surface of the prism and cannot reach region III for TI. Furthermore, the measured acoustic intensity field in the red squares *R7* and *R8* are presented in the right region and the measured results agree with the simulated results. Therefore, we can realize the inversion of the AAT performance by adjusting the phase distribution of the prism.

V. CONCLUSION

In conclusion, we demonstrate four types of passive phased array prisms with different AAMs. The designed prisms consist of 31 transmitted unit cells which are composed of a *n* layer SHR unit cell. The results show that, by selecting the appropriate parameter *h*₁ of the SHR unit cell, the AAT prism with a fractional bandwidth of 0.26 is obtained both numerically and experimentally in which the AAT phenomenon is attributed to the asymmetric phase distributions created by the nonparallel characteristic of exit interfaces for BI and TI. Moreover, the refraction angles of the transmitted waves for BI and TI can be manipulated by the incident frequency and the parameter *h*₁ of the SHR unit cell. Furthermore, by adjusting the parameter of the SHR unit cell in the prism, three other types of prisms with different AAMs (such as BAI, AAF, and reversed AAT) are demonstrated successively. The measured results agree well with the simulated ones. Such a passive phased array prism with asymmetric phase distributions of the exit interfaces on both sides opens an alternative paradigm for designing airborne sound devices with asymmetric manipulations (such as multifunctional

acoustic rectifiers and diodes), and has deep implications in the field of electromagnetism.

ACKNOWLEDGMENTS

This work was supported by National Natural Science Foundation of China (Grants No. 11774137, No. 11834008, and No. 51779107), Six Talent Peaks Project in Jiangsu Province (Grant No. GDZB-019) and the Jiangsu Qing Lan Project.

Y. Wang and J. P. Xia contributed equally to this work.

APPENDIX A: EXPERIMENTAL SETUP AND SAMPLE PHOTOGRAPHS

As shown in Fig. 12(a), the experimental setup and the AAT prism are placed in a planar waveguide system composed of two parallel plates (dimensions 2 m × 2 m × 1 cm). The wedge-shaped sound-absorbing foams are placed at the boundaries of the planar waveguide to realize an anechoic environment. The incident plane wave is generated from a speaker array driven by the power amplifier. The acoustic pressure field is scanned by a microphone (Brüel & Kjør type-4961) moved by a set of two-dimensional motorized linear stages (Newport: MIN300CC and ILS250CC). The other microphone is fixed toward the speaker array to measure the reference acoustic signal. The data is recorded by the Brüel & Kjør 3160-A-022 module and is analyzed by the software PULSE Labshop. Beyond that, the BAI, AAF, and reversed AAT prisms are shown in Figs. 12(b)–12(d), respectively.

APPENDIX B: PERFORMANCES OF AAT PRISM AT DIFFERENT FREQUENCIES

Figure 13 shows the simulated distributions of the acoustic intensity field induced by the prism for TI and

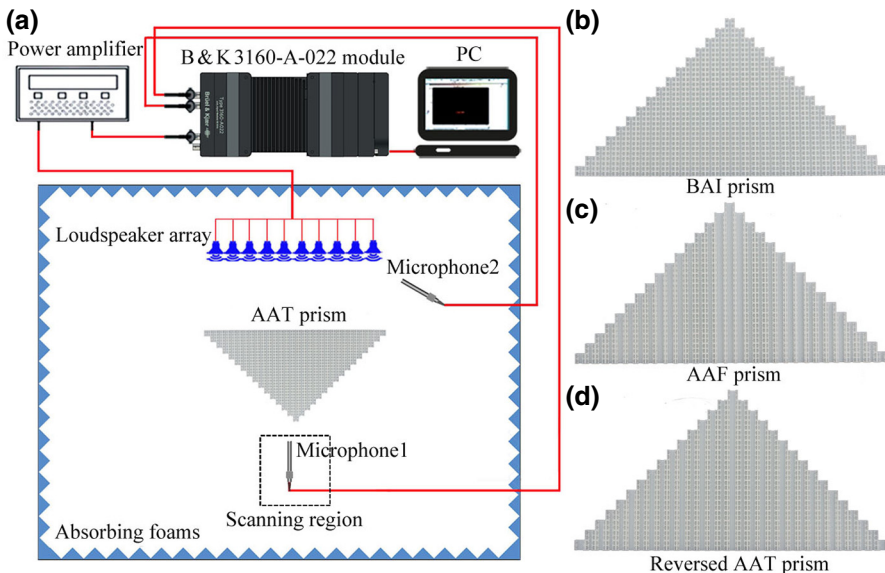


FIG. 12. (a) Experimental setup and photograph of the AAT prism. Photographs of the (b) BAI, (c) AAF, and (d) reversed AAT prisms.

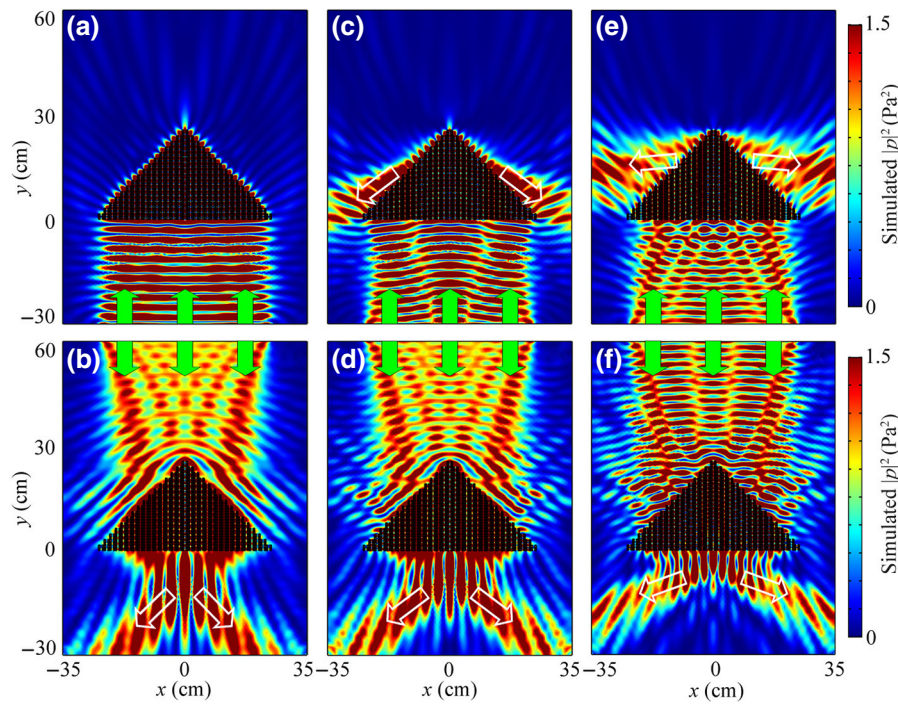


FIG. 13. Simulated distributions of acoustic intensity field induced by the AAT prism for BI and TI at (a),(b) 6.2 kHz, (c),(d) 6.7 kHz, and (e),(f) 7.2 kHz. White open and green solid arrows represent the theoretical refraction and incident directions, respectively.

BI at different incident frequencies in which the refraction angles of the transmitted waves for BI and TI match well with their theoretical ones (white open arrows) obtained from Eq. (1).

As shown in Fig. 13(a), the transmitted acoustic energy cannot pass through the prism at 6.2 kHz for BI. This is because the transmitted acoustic wave is converted into an evanescent surface wave. In addition, with the increase of the incident frequency, the transmitted acoustic energy

is not confined on both exit surfaces for BI [Figs. 13(c) and 13(e)] in which the refraction angles are in the range $-\pi/2 < \theta_{t1} < -\pi/4$. Therefore, the transmitted acoustic energy still cannot reach region I. For TI [Figs. 13(b), 13(d), and 13(f)], the acoustic wave can transmit through the prism and reach region III and the refraction angle θ_{t2} increases gradually with the increase of the incident frequency. Therefore, by changing the frequency in the working band, the AAT phenomenon still exists, but the refraction angles of the transmitted waves for BI and TI change simultaneously.

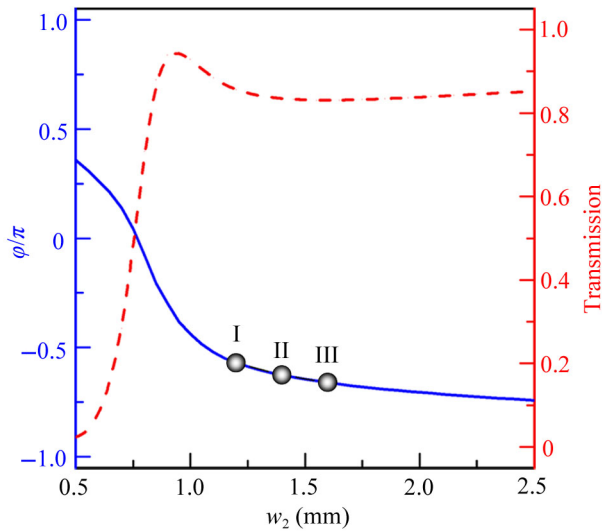


FIG. 14. Phase delays (blue solid line) and transmissions (red dashed line) of a single SHR unit cell with different values of h_1 at 6.66 kHz. The black dots I, II, and III correspond to $w_2 = 1.2$, 1.4, and 1.6 mm, respectively.

APPENDIX C: PERFORMANCES OF AAT PRISM WITH DIFFERENT PARAMETER w_2

To discuss the influence of the parameter w_2 of the SHR unit cell on the AAT performance, we simulate the phase delays (blue solid line) and transmissions (red dashed line) of a single SHR unit cell with different values of w_2 at 6.66 kHz, which are shown in Fig. 14. Note that with the increase of w_2 , the phase delay decreases gradually and the transmissions are larger than 0.8 in the range $0.8 \leq w_2 \leq 2.5$ mm. Therefore, by changing the parameter w_2 , the AAT performance can be manipulated.

Figure 15 shows the distributions of the acoustic intensity field for BI and TI with three different values of w_2 (black dots I, II, and III in Fig. 14). It is found that the AAT effect still exists with the increase of w_2 . For BI [Figs. 15(a), 15(c) and 15(e)], with the increase of w_2 , the refraction angles θ_{t1} decrease gradually, but the transmitted acoustic energy cannot reach region I. In the case of TI [Figs. 15(b), 15(d) and 15(f)], the acoustic

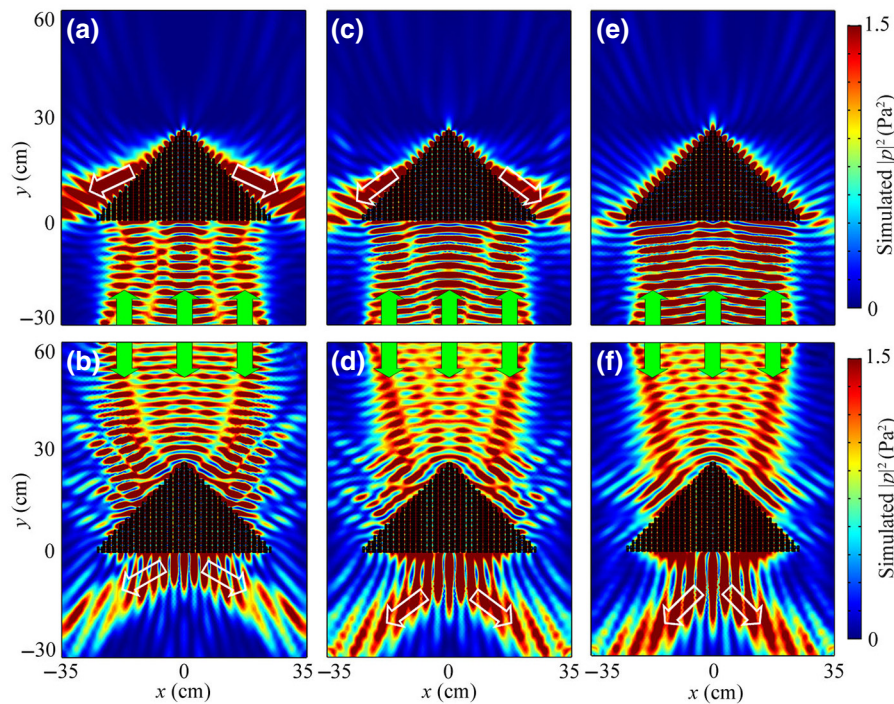


FIG. 15. Simulated distributions of acoustic intensity field induced by the AAT prism for BI and TI with $w_2 =$ (a), (b)1.2, (c), (d)1.4, and (e), (f)1.6 mm at 6.66 kHz. White open and green solid arrows represent the theoretical refraction and incident directions, respectively.

waves can transmit through the prism and reach region III and the refraction angle θ_{12} decreases gradually with the increase of w_2 . The refraction angles of the transmitted waves agree well with the theoretical angles (white open arrows). Therefore, the refraction angles for BI and TI can be manipulated by the parameter w_2 .

[1] Z. Yu and S. Fan, Complete optical isolation created by indirect interband photonic transitions, *Nat. Photonics* **3**, 91 (2009).
 [2] L. Bi, J. Hu, P. Jiang, D. H. Kim, G. F. Dionne, L. C. Kimerling, and C. A. Ross, On-chip optical isolation in monolithically integrated non-reciprocal optical resonators, *Nat. Photonics* **5**, 758 (2011).
 [3] A. Kamal, J. Clarke, and M. H. Devoret, Noiseless non-reciprocity in a parametric active device, *Nat. Phys.* **7**, 311 (2011).
 [4] M. S. Kang, A. Butsch, and P. S. J. Russell, Reconfigurable light-driven opto-acoustic isolators in photonic crystal fibre, *Nat. Photonics* **5**, 549 (2011).
 [5] D. W. Wang, H. T. Zhou, M. J. Guo, J. X. Zhang, J. Evers, and S. Y. Zhu, Optical Diode Made from a Moving Photonic Crystal, *Phys. Rev. Lett.* **110**, 093901 (2013).
 [6] D. L. Sounas, C. Caloz, and A. Alù, Giant non-reciprocity at the subwavelength scale using angular momentum-biased metamaterials, *Nat. Commun.* **4**, 2407 (2013).
 [7] L. Chang, X. S. Jiang, S. Y. Hua, C. Yang, J. M. Wen, L. Jiang, Y. L. Guan, G. Z. Wang, and M. Xiao, Parity–time symmetry and variable optical isolation in active–passive-coupled microresonators, *Nat. Photonics* **8**, 524 (2014).

[8] F. Ruesink, M. A. Miri, A. Alù, and E. Verhagen, Nonreciprocity and magnetic-free isolation based on optomechanical interactions, *Nat. Commun.* **7**, 13662 (2016).
 [9] M. Soljačić, C. Luo, J. D. Joannopoulos, and S. Fan, Non-linear photonic crystal microdevices for optical integration, *Opt. Lett.* **28**, 637 (2003).
 [10] S. Lepri and G. Casati, Asymmetric Wave Propagation in Nonlinear Systems, *Phys. Rev. Lett.* **106**, 164101 (2011).
 [11] I. V. Shadrivov, V. A. Fedotov, D. A. Powell, Y. S. Kivshar, and N. I. Zheludev, Electromagnetic wave analogue of an electronic diode, *New J. Phys.* **13**, 033025 (2011).
 [12] L. Fan, J. Wang, L. T. Varghese, H. Shen, B. Niu, Y. Xuan, A. M. Weiner, and M. H. Qi, An all-silicon passive optical diode, *Science* **335**, 447 (2012).
 [13] B. Liang, X. S. Guo, J. Tu, D. Zhang, and J. C. Cheng, An acoustic rectifier, *Nat. Mater.* **9**, 989 (2010).
 [14] N. Boechler, G. Theochari, and C. Daraio, Bifurcation-based acoustic switching and rectification, *Nat. Mater.* **10**, 665 (2011).
 [15] B. I. Popa and S. A. Cummer, Non-reciprocal and highly nonlinear active acoustic metamaterials, *Nat. Commun.* **5**, 3398 (2014).
 [16] R. Fleury, D. L. Sounas, C. F. Sieck, M. R. Haberman, and A. Alù, Sound isolation and giant linear nonreciprocity in a compact acoustic circulator, *Science* **343**, 516 (2014).
 [17] A. B. Khanikaev, R. Fleury, S. H. Mousavi, and A. Alù, Topologically robust sound propagation in an angular-momentum-biased graphene-like resonator lattice, *Nat. Commun.* **6**, 8260 (2015).
 [18] Z. Yang, F. Gao, X. Shi, X. Lin, Z. Gao, Y. Chong, and B. L. Zhang, Topological Acoustics, *Phys. Rev. Lett.* **114**, 114301 (2015).
 [19] X. Ni, C. He, X. C. Sun, X. P. Liu, M. H. Lu, L. Feng, and Y. F. Chen, Topologically protected one-way edge mode in

- networks of acoustic resonators with circulating air flow, *New J. Phys.* **17**, 053016 (2015).
- [20] Y. J. Ding, Y. G. Peng, Y. F. Zhu, X. D. Fan, J. Yang, B. Liang, X. F. Zhu, X. G. Wan, and J. C. Cheng, Experimental Demonstration of Acoustic Chern Insulators, *Phys. Rev. Lett.* **122**, 014302 (2019).
- [21] C. C. Lu, X. Y. Hu, Y. B. Zhang, Z. Q. Li, X. A. Xu, H. Yang, and Q. H. Gong, Ultralow power all-optical diode in photonic crystal heterostructures with broken spatial inversion symmetry, *Appl. Phys. Lett.* **99**, 051107 (2011).
- [22] A. Cicek, M. B. Yucel, O. A. Kaya, and B. Ulug, Refraction-based photonic crystal diode, *Opt. Lett.* **37**, 2937 (2012).
- [23] C. Wang, X. L. Zhong, and Z. Y. Li, Linear and passive silicon optical isolator, *Sci. Rep.* **2**, 674 (2012).
- [24] A. E. Serebryannikov, E. Ozbay, and S. Nojima, Asymmetric transmission of terahertz waves using polar dielectrics, *Opt. Express* **22**, 3075 (2014).
- [25] F. T. Gundogdu, A. E. Serebryannikov, A. O. Cakmak, and E. Ozbay, Asymmetric transmission in prisms using structures and materials with isotropic-type dispersion, *Opt. Express* **23**, 24120 (2015).
- [26] X. F. Li, X. Ni, L. Feng, M. H. Lu, C. He, and Y. F. Chen, Tunable Unidirectional Sound Propagation Through a Sonic-Crystal-Based Acoustic Diode, *Phys. Rev. Lett.* **8**, 084301 (2011).
- [27] Y. Li, J. Tu, B. Liang, X. S. Guo, D. Zhang, and J. C. Cheng, Unidirectional acoustic transmission based on source pattern reconstruction, *J. Appl. Phys.* **112**, 064504 (2012).
- [28] Z. J. He, S. S. Peng, Y. T. Ye, Z. W. Dai, C. Y. Qiu, M. Z. Ke, and Z. Y. Liu, Asymmetric acoustic gratings, *Appl. Phys. Lett.* **98**, 083505 (2011).
- [29] H. Jia, M. Z. Ke, C. H. Li, C. Y. Qiu, and Z. Y. Liu, Unidirectional transmission of acoustic waves based on asymmetric excitation of Lamb waves, *Appl. Phys. Lett.* **102**, 153508 (2013).
- [30] H. X. Sun, S. Q. Yuan, and S. Y. Zhang, Asymmetric acoustic transmission in multiple frequency bands, *Appl. Phys. Lett.* **107**, 213505 (2015).
- [31] A. Cicek, O. A. Kaya, and B. Ulug, Refraction-type sonic crystal junction diode, *Appl. Phys. Lett.* **100**, 111905 (2012).
- [32] J. H. Oh, H. W. Kim, P. S. Ma, H. M. Seung, and Y. Y. Kim, Inverted bi-prism phononic crystals for one-sided elastic wave transmission applications, *Appl. Phys. Lett.* **100**, 213503 (2012).
- [33] B. Yuan, B. Liang, J. C. Tao, X. Y. Zou, and J. C. Cheng, Broadband directional acoustic waveguide with high efficiency, *Appl. Phys. Lett.* **101**, 043503 (2012).
- [34] R. Q. Li, B. Liang, Y. Li, W. W. Kan, X. Y. Zou, and J. C. Cheng, Broadband asymmetric acoustic transmission in a gradient-index structure, *Appl. Phys. Lett.* **101**, 263502 (2012).
- [35] Y. L. Huang, H. X. Sun, J. P. Xia, S. Q. Yuan, and X. L. Ding, Multi-band asymmetric acoustic transmission in a bended waveguide with multiple mechanisms, *Appl. Phys. Lett.* **109**, 013501 (2016).
- [36] Y. Li, B. Liang, Z. M. Gu, X. Y. Zou, and J. C. Cheng, Unidirectional acoustic transmission through a prism with near-zero refractive index, *Appl. Phys. Lett.* **103**, 053505 (2013).
- [37] A. L. Song, T. N. Chen, X. P. Wang, and Y. H. Xi, Broadband asymmetric acoustic transmission through an acoustic prism, *Phys. Lett. A* **381**, 2283 (2017).
- [38] Y. Li, B. Liang, Z. M. Gu, X. Y. Zou, and J. C. Cheng, Reflected wavefront manipulation based on ultrathin planar acoustic metasurfaces, *Sci. Rep.* **3**, 2546 (2013).
- [39] Y. B. Xie, W. Q. Wang, H. Y. Chen, A. Konneker, B. I. Popa, and S. A. Cummer, Wavefront modulation and sub-wavelength diffractive acoustics with an acoustic metasurface, *Nat. Commun.* **5**, 5553 (2014).
- [40] K. Tang, C. Y. Qiu, M. Z. Ke, J. Y. Lu, Y. T. Ye, and Z. Y. Liu, Anomalous refraction of airborne sound through ultrathin metasurfaces, *Sci. Rep.* **4**, 6517 (2014).
- [41] Y. F. Zhu, Z. M. Gu, B. Liang, J. Yang, J. Yang, L. L. Yin, and J. C. Cheng, Asymmetric sound transmission in a passive non-blocking structure with multiple ports, *Appl. Phys. Lett.* **109**, 103504 (2016).
- [42] Y. Ge, H. X. Sun, S. Q. Yuan, and Y. Lai, Broadband unidirectional and omnidirectional bidirectional acoustic insulation through an open window structure with a metasurface of ultrathin hooklike meta-atoms, *Appl. Phys. Lett.* **112**, 243502 (2018).
- [43] Y. Ge, H. X. Sun, S. Q. Yuan, and Y. Lai, Switchable omnidirectional acoustic insulation through open window structures with ultrathin metasurfaces, *Phys. Rev. Mater.* **3**, 065203 (2019).
- [44] C. Shen, Y. B. Xie, J. F. Li, S. A. Cummer, and Y. Jing, Asymmetric acoustic transmission through near-zero-index and gradient-index metasurfaces, *Appl. Phys. Lett.* **108**, 223502 (2016).
- [45] X. Jiang, B. Liang, X. Y. Zou, J. Yang, L. L. Yin, J. Yang, and J. C. Cheng, Acoustic one-way metasurfaces: Asymmetric phase modulation of sound by subwavelength layer, *Sci. Rep.* **6**, 28023 (2016).
- [46] J. P. Xia, X. T. Zhang, H. X. Sun, S. Q. Yuan, J. Qian, and Y. Ge, Broadband Tunable Acoustic Asymmetric Focusing Lens From Dual-Layer Metasurfaces, *Phys. Rev. Appl.* **10**, 014016 (2018).
- [47] Y. Li, C. Shen, Y. B. Xie, J. F. Li, W. Q. Wang, S. A. Cummer, and Y. Jing, Tunable Asymmetric Transmission via Lossy Acoustic Metasurfaces, *Phys. Rev. Lett.* **119**, 035501 (2017).
- [48] B. Y. Xie, H. Cheng, K. Tang, Z. Y. Liu, S. Q. Chen, and J. G. Tian, Multiband Asymmetric Transmission of Airborne Sound by Coded Metasurfaces, *Phys. Rev. Appl.* **7**, 024010 (2017).
- [49] N. Yu, P. Genevet, M. A. Kats, F. Aieta, J. P. Tetienne, F. Capasso, and Z. Gaburro, Light propagation with phase discontinuities: generalized laws of reflection and refraction, *Science* **334**, 333 (2011).
- [50] See Supplemental Material <http://link.aps.org/supplemental/10.1103/PhysRevApplied.12.024033> for the design and performances of a BAI prism with $d\varphi_2/kdx_2 = 1.0$, the 16 discrete phase delays of the transmitted unit cells for the AAF prism, the phase gradient $d\varphi_1/kdx_1$ of the AAF prism, the 16 discrete phase delays of the transmitted unit cells for the reversed AAT prism, and the design and performances of the reversed AAT prism with $d\varphi_2/kdx_2 = -1.0$.